

Chapter 6

3D-Printed Microoptics by Femtosecond Direct Laser Writing



Simon Thiele and Alois Herkommer

Abstract Femtosecond direct laser writing offers unique possibilities for the fabrication of microoptical components and systems. Almost unrestricted 3D design freedom, high resolution and accuracy, as well as alignment-free assembly enable direct printing of complex structures with optical functionality. Various imaging and illumination optics are presented and discussed (Most of the contents shown are a directly translated from the PhD thesis “Design, Simulation und Prozessoptimierung für das 3D-Laserdirektschreiben von Mikrooptiken” by Simon Thiele, University of Stuttgart (2019)).

Keywords Laser direct writing · Microoptical components · Freeform design · High-resolution printing · Imaging optics · Illumination optics · Two-photon lithography · 3D lithography

6.1 Introduction

Microoptical components have nowadays found their way into almost all areas of our lives and have become indispensable in technology sectors such as communications technology, medical technology, sensor technology, or consumer electronics. Examples include microlenses for beam shaping in fiber optics, small endoscope lenses for minimal invasive surgery, microlens arrays for the homogenization of laser illumination, and the tiny imaging lens systems in the cameras of our smartphones.

The microoptics of today mainly emerged from semiconductor manufacturing in the 1970s and 1980s and would most likely not be as widespread without this important technological driver. Some paradigms of this industry, such as high parallelism, high throughput, and cost reduction through miniaturization, have influenced microoptics and clearly distinguish it from the traditional categories of the optical industry.

S. Thiele · A. Herkommer (✉)

Institute of Applied Optics (ITO) and Research Center SCoPE, Stuttgart, Germany

e-mail: alois.herkommer@ito.uni-stuttgart.de

© Springer Nature Switzerland AG 2021

A. Heinrich (ed.), *3D Printing of Optical Components*, Springer Series in Optical Sciences 233, https://doi.org/10.1007/978-3-030-58960-8_6

239

An interesting mixture of both worlds can be observed in the lenses of today's smartphones. Here, too, highly automated work is carried out with low-cost materials (polymers) and low-cost processes (injection molding/injection stamping), although the result is complex and consists of many precisely aligned individual components. The optical performance requirements in the case of smartphone cameras demand complex meniscus aspheric shapes, not accessible through wafer-based processes as they allow only limited surface complexity and have so far not been able to assert themselves despite their advantageous cost structure. However, there are clear downward limits to the methods of assembling replicated lens components, as alignment and assembly become more and more difficult with increasing miniaturization. New methods must be developed in order to transfer the complexity of smartphone lenses and other microoptical systems to smaller scales.

One of the most promising candidates for the fabrication of next-generation microoptics is additive manufacturing using multiphoton lithography as it is inherently alignment-free and allows for extreme miniaturization as well as almost unrestricted design freedom. Figure 6.1 compares all three methods based on the assessment of the authors.

The generative fabrication of microoptics in the sense of 3D printing is a comparatively young field of research. Classical methods, such as direct laser writing, have been used for decades to fabricate microoptics, but the layer-by-layer printing

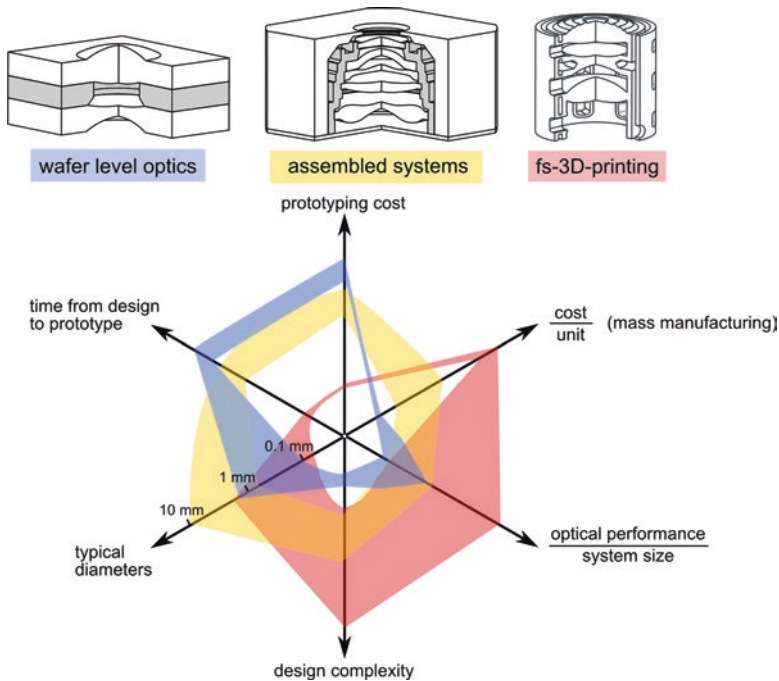


Fig. 6.1 Comparison of different technologies for the fabrication of microoptical systems according to the author's assessment

of three-dimensional structures did not become established until the mid-2000s. An important driver of this technology was the development of multiphoton lithography with first publications in the late 1990s [1–3].

As some of the first structures with optical functionality photonic crystals were fabricated [4–13]. In order to use these crystals in the visible spectrum with high efficiency, finest structure sizes must be realized. Therefore, the method was further improved by using stimulated emission depletion (STED) approaches to reach voxel sizes down to the range of a few 10 nm [14, 15]. To produce smooth surfaces and monolithic components, however, the voxel size is less important, and photore-sists with a stronger proximity effect are desired, since rounding attenuates staircase effects. The latter can also be achieved by a specific surface treatment after printing [16].

First microoptical components such as microprisms, waveguides, or microlenses [17–21] were demonstrated in the mid-2000s. In the following years, a number of research papers were published presenting diffractive lenses [22], microlenses (and arrays) [23–27], diffractive-refractive hybrid lenses [28], vortex lenses [29, 30], multifocal lenses [31], pattern generators [32], ring resonators [33, 34] or freeform lenses [35, 36].

Multielement systems in which the components are arranged along the optical axis have also been published several times [37–41]. Due to their built-in microscope, multiphoton lithography setups usually allow a very accurate adaption and alignment of the writing process to the substrate. Therefore, soon the first elements were printed on the tip of optical fibers. In addition to refractive and reflecting surfaces for beam shaping [39, 42–44], photonic crystals [37, 45], phase plates [46, 47], or moth-eye structures for reflex suppression [48] were written directly on fibers. As an alternative to direct printing, a clip-on approach can also be chosen [49]. Other substrates such as optical crystals [50] or image sensors [40] can also be used for printing.

While classical photopolymers are typically used as writing materials, hybrid organic-inorganic polymers [51], proteins [52], or even glass [53] is also used.

Other generative manufacturing processes comparable to multiphoton lithography have so far been limited to inkjet-based approaches [54] and ablative processing of photosensitive glass [55]. In terms of optical functionality, however, the demonstrated components have so far been less mature in comparison.

The fabrication of planar optical elements by single-photon laser direct writing goes back to works from the early 1980s [56]. At that time, semiconductor processes were adapted in order to lithographically generate optical structures such as microlens arrays or diffractive elements directly without any mask. The employed photosensitive (UV) resist typically shows a linear relation between light intensity and chemical structural change. The photon absorption can lead to either a polymerization (negative resist) or to a local de-bonding (positive resist) and thus together with a development step planar structures can be fabricated.

In addition to linear single-photon absorption, nonlinear absorption mechanisms, also known as two- or multiphoton absorption, exist which were first described in the early 1930s [57]. However, due to the extreme photon densities required, this

approach required the invention of the laser to be realized experimentally. The development of the titanium-sapphire femtosecond laser [58, 59], which fulfilled the requirements for novel experiments for the first time, is regarded as an important breakthrough for this technology. The dependence of the transition rate on the squared intensity is a great advantage with regard to three-dimensional lithography, since absorption processes can be confined to a very small area (focus).

In the case of two-photon lithography, light from the near infrared is typically used together with a photoresist, which is photosensitive at $\lambda/2$, i.e., mostly in the UV spectral range. The simultaneous absorption of two photons (see Fig. 6.2—right) produces free radicals from so-called photoinitiator molecules, which break double bonds and thus initiate polymerization. This is temporally and spatially limited and results in a so-called voxel of polymerized material at the focal spot.

Usually a voxel has the shape of an ellipsoid and has, depending on the numerical aperture with which it is focused, a varying size and a varying aspect ratio. Even in the case of strong focusing in immersion (e.g., with a numerical aperture of 1.4), an aspect ratio of at least 2.7 remains without further manipulation of the wavefront. The minimum dimensions of the voxels are typically about 100 nm in width and 270 nm in length. Complex three-dimensional objects are created line by line and layer by layer in a mostly liquid photoresist, which remains transparent in the visible spectrum after polymerization. Figure 6.2 schematically shows the functional principle of this method.

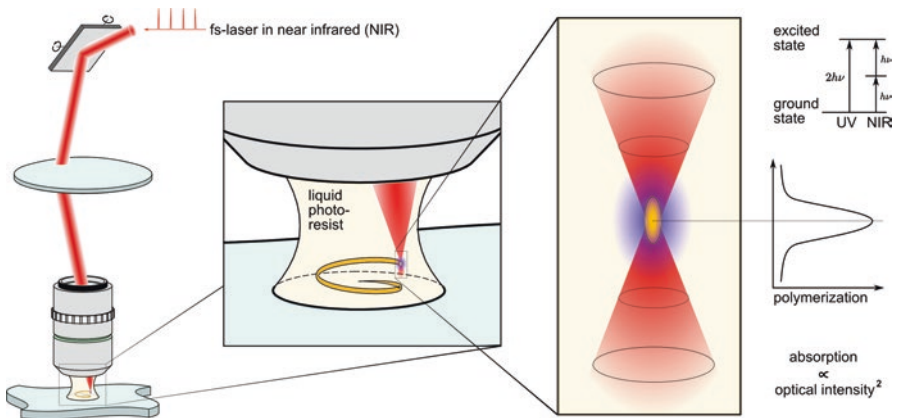


Fig. 6.2 Schematic setup for two-photon lithography. A microscope is dipped into a photoresist fluid. The laser focus is then moved via the galvo scanner within the fluid to locally polymerize the material

6.2 Design Rules for 3D-Printed Microoptics

The above-described printing process and the current limitations of the printing device result in some general and specific design rules, which should be considered during optical design, structural design, and process development.

Limited Printing Volume

The maximum printable volume is limited by the lithography device architecture and by the writing time, which is usually critical due to the small voxel size. Therefore, the size of the solid printed optical elements should be minimized as far as possible. Usually, the total size of the printed system is in the range of below 1 mm in each dimension.

Geometry Restrictions

Due to the small voxel size in vertical direction the printing process allows comparably small lens thicknesses of down to 5 μm . Edge thicknesses close to the structural mount should be thicker. For air gaps between elements, larger distances must be maintained to ensure that remaining photoresist can be reliably washed out.

Elimination of Alignment Tolerances

The complete optical system, including all elements and mechanical support structure, can be printed in one single process. In consequence, there are no alignment or mounting tolerances which need to be considered. The only remaining tolerance effect is the printing accuracy of the lithographic printing itself, which is well below 1 μm in all three dimensions. With a certain pre-knowledge and compensation of the shrinkage of the resist, the absolute geometry accuracy can even be smaller.

Mono-material

The printing of a combination of materials, e.g., different dispersion for chromatic corrections, is possible in general and has already been demonstrated. However, two materials require additional effort and writing time and may introduce alignment errors. Therefore, it is rational and economic to limit the material choice to only one polymer material, if possible. The standard photoresist employed for the following examples is IP-S (Nanoscribe GmbH, Germany), with a refractive index of $n = 1.5\text{--}1.54$ in the visible range. For coarse design estimates, we use a refractive index of $n = 1.5$.

Properties of Polymer Optics

The polymer-based printing materials typically exhibit a few disadvantages. For example, the range of materials and thus the available refractive indices as well as Abbe numbers is rather limited. Polymers are also more sensitive to temperature changes, are more difficult to coat, and offer less mechanical and chemical stability. Moreover stress-induced birefringence can be a problem.

Avoiding Ray Bending

In imaging optical design, it is good practice to avoid strong ray bending, a term which usually describes high angles between rays and the local surface normal at their point of incidence or exitance in air or glass. These angles are illustrated in Fig. 6.3 as γ_L and γ_G , respectively. High angles usually introduce large aberrations, which must be compensated elsewhere. Such systems are therefore sensitive to small changes and fabrication tolerances [60–62]. Furthermore, increasing ray bending leads to an increase in dielectric losses. This leads to transmission loss and enhanced stray light in the system. Therefore, a maximum local angle of incidence is typically included into the optimization merit function. In the example imaging optical systems shown below, we have limited the allowed maximum angle towards air to approximately 56.3° (Brewster’s angle).

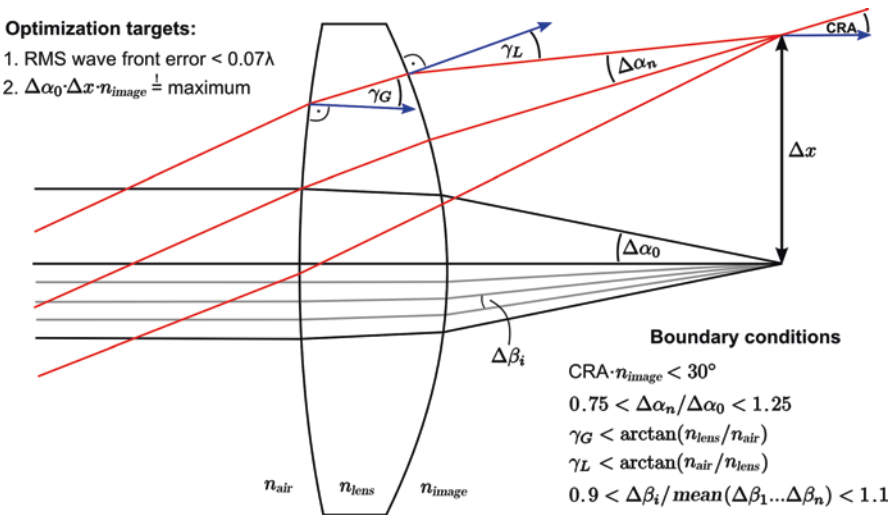


Fig. 6.3 Typical design targets and boundary conditions for the design of 3D printable highly aspherical lens systems

Avoiding Large Chief Ray Angles (CRA)

In most modern optical application, the microoptical system is used together with a CMOS image sensor or an imaging fiber bundle. Both elements do not allow large chief ray angles (CRA) in the image space. This angle is illustrated in Fig. 6.3. Usually the maximum CRA must be controlled below 30° for CMOS chips and below 20° for imaging fibers. In the following designs, we limit the CRA to 30° in air, or to $30^\circ/n$ if the image space is immersed with a material of refractive index n .

Realization of Strong Aspheres and Freeform Surfaces

The printing process basically allows creating any 3D geometry, not only for the structural mount but also for the optical surfaces. In consequence, the limitation to classical optical surface shapes, such as rotational symmetric spheres, no longer exists. 3D printing naturally allows for aspheric or even freeform surfaces with large asphericity in the optical design. As a result of the added degrees of freedom, the performance of a design can be improved while keeping the same (or smaller) number of elements, and often also the total built volume can be significantly reduced.

In order to verify this hypothesis, we have compared the achievable performance of spherical to aspherical systems. As a performance figure of merit, we have compared the achievable space-bandwidth product of the designs, which connected to the product of the marginal ray angle $\Delta\alpha_0$ and the field size Δx , inside which the performance can be corrected to be diffraction limited. Figure 6.4 shows the resulting designs for 1–6 spherical surfaces in the upper row and 1–6 aspherical surfaces (with polynomial coefficients up to the tenth order) in the lower row. Below the merit function of the designs is illustrated.

From the design study and analysis, we find an almost linear dependence between the number of optical surfaces and the achievable figure of merit. From this behavior it may be concluded that all systems have been corrected to the same final level. The other main finding is that aspheric surfaces allow for a larger gradient of this dependence. This nicely verifies that aspheres provide a clear benefit for the achievable optical performance in terms of an increased space-bandwidth product as compared to an all-spherical design. However, it has to be noted that this dependence cannot be generalized to other design problems, as here the abovementioned boundary conditions on maximum incidence angles and CRA have been considered during the design.

The space-bandwidth product can also be converted into the number of resolvable image points. This number can be calculated from the maximum diffraction limited field size, divided by the diameter of the Airy disk, according to the Rayleigh criterion. The resulting quadratic dependence in Fig. 6.4 relative to the linear dependence of the space-bandwidth product results from the fact that the pixel number scales with the area (quadratic in field size).

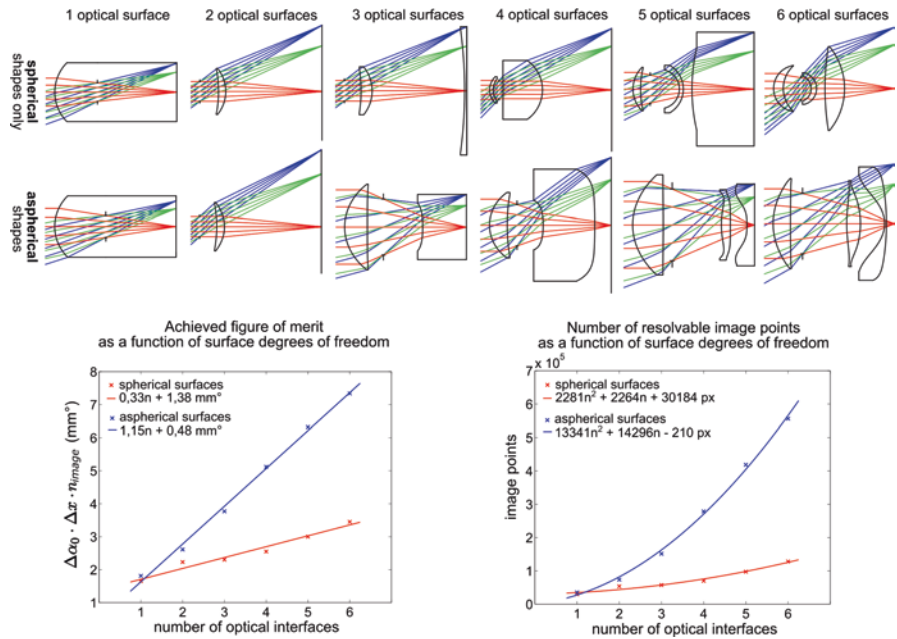


Fig. 6.4 Comparison of optimized spherical designs (upper row) versus aspherical designs (lower row) for an increasing number of surfaces. Below the corresponding space-bandwidth product is illustrated (left) and the respective number of resolvable image points (right)

Integration of Diffractive Structures

In addition to aspheric and freeform surfaces, multiphoton lithography, due to the small voxel size in lateral direction, allows for a direct printing of diffractive structures. These can add additional degrees of freedom and thus further improve the optical performance. In addition, the small size of the components does typically not require high line densities, which helps to avoid otherwise typical losses in diffraction efficiency. In general, diffractive elements are very useful in optical design, as they can not only compensate first-order chromatic aberrations, but also third-order monochromatic aberrations. These advantages must be compared to the well-known disadvantages of wavelength-dependent diffraction efficiency, large dispersion, and unavoidable residual light into unwanted diffraction orders.

Wave-Optical Effects

Diffractive elements are a prime example why a wave-optical analysis of the system is recommended as it allows for calculation of diffraction efficiency and chromatic effects. However, even without diffractive structures, the size of the printed elements is often small enough that diffraction effects from the apertures must be considered. As a criterion the so-called Fresnel number can be used. A significant

diffraction effect must be expected when the Fresnel number approaches unity. It is known that in this case, diffraction will lead to an effective reduction of the focal length, or to diffraction-stimulated chromatic effects [63].

6.3 Examples of Printed Microoptical Imaging Systems

The following two examples of printed imaging systems shall illustrate the applications and limitations of 3D printing processes for optics in more detail.

Both systems have been optimized for 3D printing under the abovementioned design rules. In order to take full advantage of the high accuracy of the process, the design should be optimized such that it can be printed in one step, without any assembly or realignment. Moreover, openings in the structure and distances between the elements must be chosen such that the photoresist can be properly washed out. The latter condition is directly influencing the optical design.

In prior work it turned out that for uncoated surfaces, a surface number of 4, i.e., two aspheric lens elements, is a good compromise of optical quality and transmission loss. Fewer surfaces do not allow for a large enough space-bandwidth product, and more surfaces introduce too much material absorption, reflection losses, and stray light. Both designs have been furthermore optimized for IP-S photoresist, as mentioned above. The dispersion characteristics of IP-S were accurately measured over the visible range and included into the optical design software ZEMAX. The employed lithographic printing system (Nanoscribe GT Professional, Nanoscribe GmbH, Germany) at that time supported two different writing objectives and field diameters to be printed: a maximum diameter of 200 μm for the 63x objective and 500 μm for a 25x objective. In consequence the diameters of the optical systems were limited to 125 μm , respectively 450 μm . From the scaling laws of optical systems, it is known that smaller systems are easier to correct, since geometric and axial chromatic aberrations scale down with size. In addition, shrinkage effects of the polymer resist have less impact if the lens is smaller. Since the manufacturing of absorbing aperture stops (see later in this chapter) was not available at that time, both designs have their stop at the front surface. The image plane is located exactly at the substrate interface on which the print is fixed.

The two designs are microoptical versions of a tele-system (diameter 125 μm , field of view 20°) and a distortion corrected camera lens (diameter 450 μm , field of view 40°). Table 6.1 lists the most important parameters of both systems. In both systems aspheric surfaces are used, even if the asphericity is not strikingly visible in the lens drawing.

For the listed number of resolvable image points, the field of view was divided into five zones with equal area. In each zone the average radius of the Airy disk is used, if the image quality is diffraction limited, whereas the geometrical spot radius is used if geometrical aberrations are limiting.

Both designs are well corrected for distortion, which usually is additional effort or comes at the cost of other aberrations. This is one of the reasons why the camera

Table 6.1 Comparison of the two printed imaging systems, with four surfaces

Variant	Micro tele-lens	Camera lens
Aperture diameter	97 μm	390 μm
Maximum lens diameter	97 μm	390 μm
Length	204 μm	650 μm
Focal length	261 μm	544 μm
Full field of view	20°	40°
Numerical aperture (image space)	0.2	0.37
Object distance	∞	∞
Distortion	-0.1%	1%
Number of resolvable Image points	~2500	~40,000

lens could not be corrected to be diffraction limited over the full field of view at the employed f-number of 1.35. However still the number of resolvable pixels is much higher, and the spot size is smaller as compared to the tele-lens. Moreover, the absolute amount of light is larger due to the larger diameter. Figure 6.5 shows the optical layout of both designs.

After finishing the optical design, the surfaces are exported either via ZEMAX or via the mathematical surface description to a computer-aided design (CAD) model. In the CAD software (e.g., SolidWorks), the appropriate mechanical support structure is added, as illustrated in Fig. 6.6.

The height of the support structure is designed such that the image plane is exactly positioned on the substrate, which usually is a cover glass. If the lenses have convex shapes towards the bottom of the system, special care must be taken to print the vertex without them swimming in the resist.

Before the final printing process, CAD models must be triangulated and converted into a STL format. From that file the software “DeScribe “ (Nanoscribe GmbH) creates a machine-readable format, which among other parameters contains the writing trajectories, as well as laser power, scan speed, and delay times.

The physical printing process is then performed using the “Dip-In” configuration with the 63 \times /1.4 NA objective (for the tele-lens) and the 25 \times /0.8 NA objective for the camera lens. The typical writing time is in the range of 2–3 h. After resist development and washout of the unused resist, the results are typically inspected with a digital microscope (Keyence VHX-1000), in order to assess the quality of the print. Figure 6.7 shows images of a print in comparison. However, this inspection only allows a qualitative first assessment.

For a more quantitative assessment of the imaging performance, a microscope arrangement can be employed. Here an object is imaged through the printed microoptics, and the created intermediate image is observed via a microscope system on the image side. As a standard object, the USAF-1951 test target is used, which is positioned at a hyperfocal distance. The imaging results are shown in Fig. 6.8, for both objectives. The visible part of the test chart is different, as the

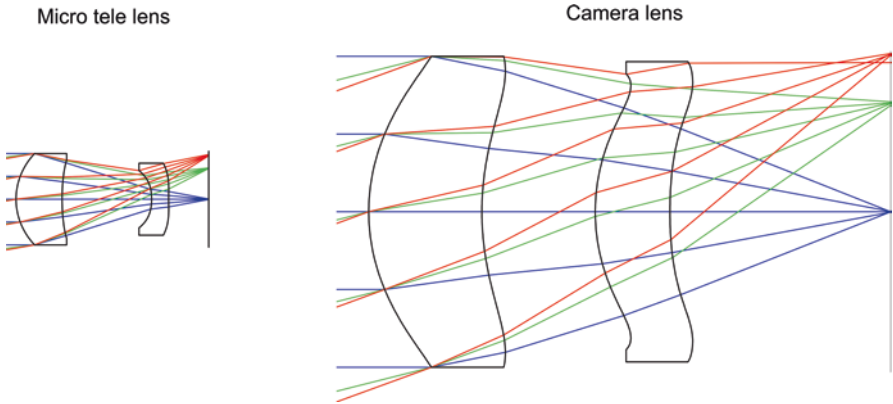


Fig. 6.5 Layout of the microoptical printed tele-lens and the camera lens

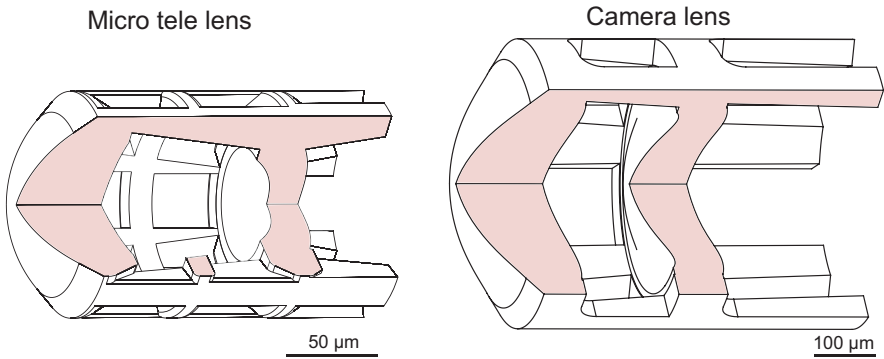


Fig. 6.6 CAD-model of the tele-lens and the camera lens including the support structure. For better visualization a quarter of the lens model has been removed

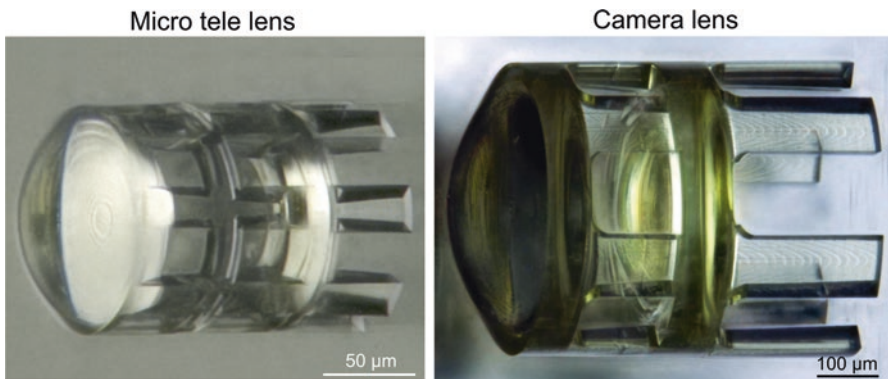


Fig. 6.7 Digital microscope image of printed version of the two designs

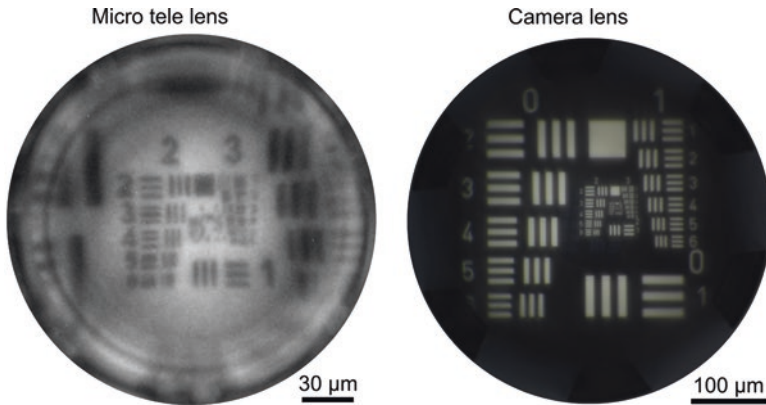


Fig. 6.8 Experimentally recorded image quality. For the camera lens, stray light was suppressed by external shielding

object is placed at different distances. However, the image quality already proves that the amount of details which can be transmitted is larger for the camera lens.

The contrast in both systems is different, since for the tele-lens, no measures for stray light suppression have been made; however the camera lens was surrounded by a black sheet of paper. This already brings us to another downside of mono-material systems. The fully transparent material of lens and mount will lead to a large amount of stray light, which even for perfect corrected systems can diminish the optical performance or even can make them useless. In consequence any optical system usually requires some way of stray light suppression, or at least a well-defined aperture. Otherwise light from undesired directions can enter the system or directly reach the image. Mono-material polymer optical system as shown above does not offer possibilities to integrate absorptive apertures, as all the material is transparent. Therefore, the optics will suffer from a loss of contrast, even if the illumination conditions are optimized. This is illustrated for another optical system as shown in Fig. 6.9. Here a fully transparent optical system, in this case a miniaturized Zeiss Hologon, is simulated via nonsequential ray tracing. The simulation drastically shows the difference between a system without any shielding, as compared to a system with absorptive walls and an absorptive aperture stop. The image simulation reveals that without stray light suppression, the contrast of the image is extremely poor which underlines the need for an integration of absorptive structures. Unfortunately, up to now no printable absorptive material is available. In addition, a second material would require an unwanted alignment step. Other possibilities are a post-process coating step [64] with an absorption layer, or the metal deposition out of a liquid suspension stimulated by the two-photon absorption [65].

Another option is the realization of refractive apertures or retro-reflective surfaces. Such elements will not absorb but rather redirect the light into uncritical directions. These structures and textures can be integrated into the printing process; however, they will work only within a limited range of incidence angles.

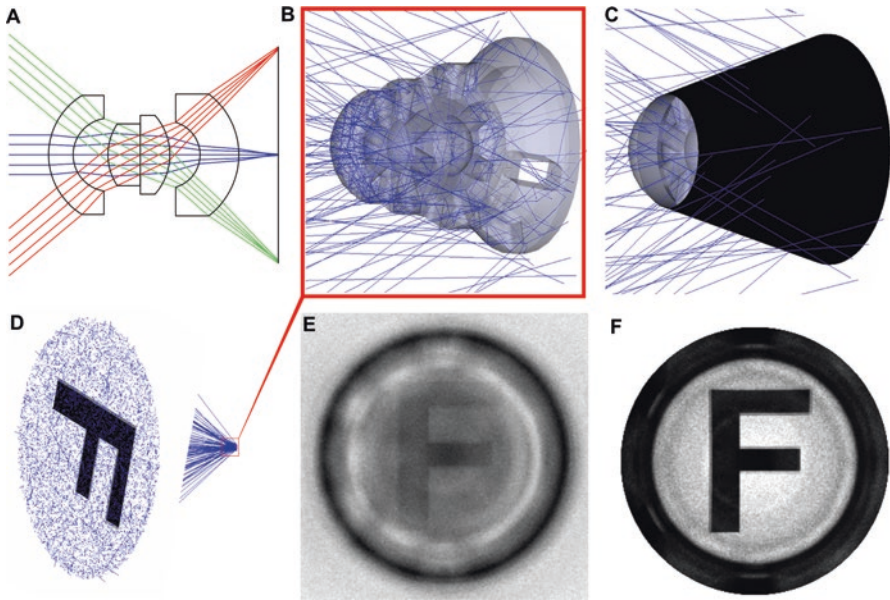


Fig. 6.9 Nonsequential ray tracing simulation of a miniaturized Zeiss Hologon. (a) Design layout. (b) Simulation for a fully transparent design. (c) Same simulation, but now with absorbing hull and absorbing aperture. (d) Employed source model for the letter “F.” (e) Simulated image of this source for the transparent version. (f) Simulated image for the absorptive model

So far, the most promising method is the integration of microfluidic channels into the 3D model. These channels can later be filled with nontransparent ink. As the channels are printed with the same process, no additional alignment error is introduced¹. The approach requires a good understanding of capillary forces, which are dominant at the microscale. Also, the choice of the liquid is important, since a large absorption is required. Metallic ink has proven to be a good candidate, as it also dries fast and can be sintered at low temperatures. The principle and corresponding manufacturing steps are illustrated in Fig. 6.10. Here a triplet lens is integrated into a special designed support structure, which is later filled with ink. The ink-filled channels form an absorptive hull, as well as an integrated aperture. Die filling process can be performed with several techniques. Either pressure is used to push the ink out of the capillary or electrical voltage. A passive technique where only the initial drop is created from a superfine inkjet printer (SIJ-S030) and the rest is self-filled via capillary forces has proven to work well. Figure 6.10 shows images of such a filling process in the lab.

The experimental results, as shown in Fig. 6.11, demonstrate the resulting improvement of contrast, this time for an endoscopic imaging system. Note that

¹This method has been patented (EP 3162549 A1) and is currently under investigation.

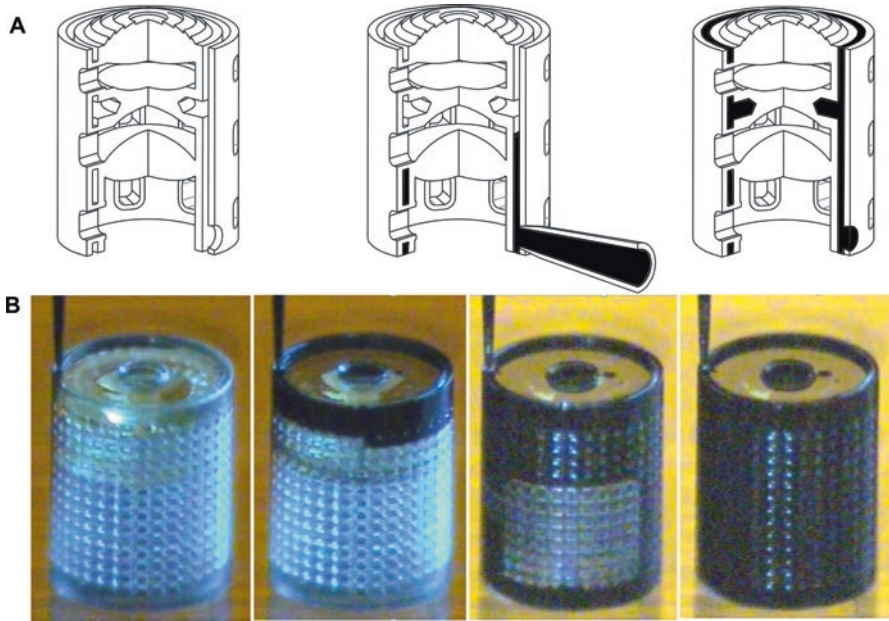


Fig. 6.10 Principle of generating absorptive structures. (a) Schematic process illustrated for a triplet with specially designed support structure. (b) Image sequence of the real filling process in the lab

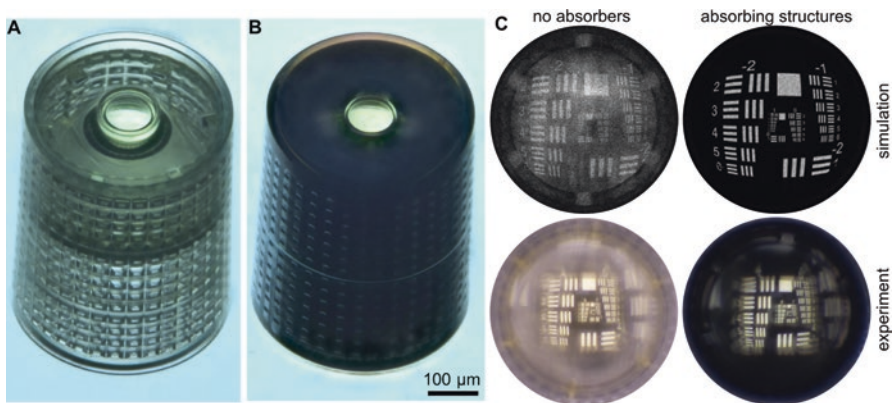


Fig. 6.11 Realized endoscopic imaging systems with absorptive elements. (a) Endoscopic system before filling with ink. (b) System after being filled with ink. (c) Comparison of the imaging results in theory and experiment

here the support hull is designed with small openings, large enough to let the ink dry, but too small to let the ink go through. The front aperture is realized by a liquid reservoir right on top of the structure. As a result of the absorptive ink, the image contrast is drastically improved in simulation, as well as in the experiment.

6.4 Printed Nonimaging Optics

The above chapter has proven that printed imaging systems are possible. However, since the geometry is not limited to refractive lenses, it is legitimate to also apply the technique for fabrication of nonimaging optical elements. Nonimaging optics describes systems which mainly collect radiation from a source volume into a target volume. In contrast to the above systems, they usually will not deliver an image from the object (source). Such systems are often employed for illumination but are also used for other purposes. Typical macroscopic applications of such systems can be found in automotive headlights, backlight displays, public lighting, flashlights, or solar collectors. On a smaller scale, corresponding elements can be found in sensors, fiber couplers, endoscopic systems, or photonic circuits.

One promising nonimaging application of direct 3D printing is the fabrication of concentration and collection systems on top of quantum dots for increased sensitivity. As the printing process allows for accurate alignment of the optics to the quantum dot, tailored freeform systems for beam shaping and collection are possible. In the following example, the printed optical system is designed to collect a large numerical aperture and collimate the light towards a secondary receiver system.

For this purpose, a two-element refractive collection system was designed with a numerical aperture of 0.7. The design was corrected for a field of view of a few micrometers, since the position of the quantum dot is only determined within certain tolerances. The quantum dot and the printed optics are contained within a cryo cell. Outside of the cryo cell, the light is captured through secondary optics with a numerical aperture 0.4. Figure 6.12 shows the design, the CAD model, and the manufactured optics.

Experimental tests at our cooperation partner have shown that the printed optics is operational at a temperature of a few degrees Kelvin and that the overall efficiency of the system can be improved significantly [66].

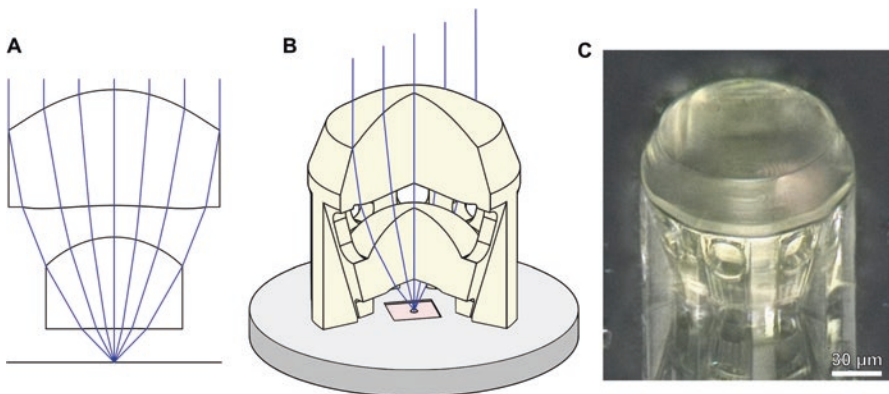


Fig. 6.12 Printed collection system on top of a quantum dot. (a) Optical design, (b) schematic setup, (c) microscope image of the printed system

Optical stimulation can, e.g., be achieved by a small laser focus. Also, for this purpose printed optical elements are of general use. For focusing narrowband light, diffractive elements can be employed which bring several advantages: the diffractive lens can be realized in a thin layer, which dramatically reduces printing volume and printing time. The thin optical volume also minimizes the material absorption and volume scattering effects, which are both known problems in some types of photoresists. Moreover, the multiphoton printing process intrinsically, due to the voxel shape, offers a higher lateral resolution as compared to the axial resolution, which is ideal for small feature sizes of the diffractive profile. General limitations of diffractive optics however are the large chromatic dispersion, the wavelength-dependent diffraction efficiency, and the limited efficiency at large deflection angles. In order to assess such limitations, a diffractive lens with a high numerical aperture of 0.8 was designed. The design of the diffractive phase profile itself is possible with any state-of-the-art optical design software in the geometrical limit, where physical optical effects, like diffraction efficiency, and multiple orders are not included. The ideal design was optimized for a wavelength of 543 nm and theoretically should deliver a diffraction limited spot. However, this is only true under the so-called thin element approximation (TEA) [67]. Even for a perfect kinoform with optimum step height, reduced diffraction efficiency is to be expected due to unavoidable self-shadowing effects for large angles.

The optimum profile step height h in air can be easily calculated via the refractive index n at the given wavelength λ to be $h = \lambda/(n - 1)$. The efficiency loss of a real profile in comparison to the ideal TME can, e.g., be simulated using the “wave propagation method” (WPM) [68].

Figure 6.13 shows the design for a diameter of 180 μm and a focal length of 67.5 μm . From the theoretical phase function, the diffractive profile and the

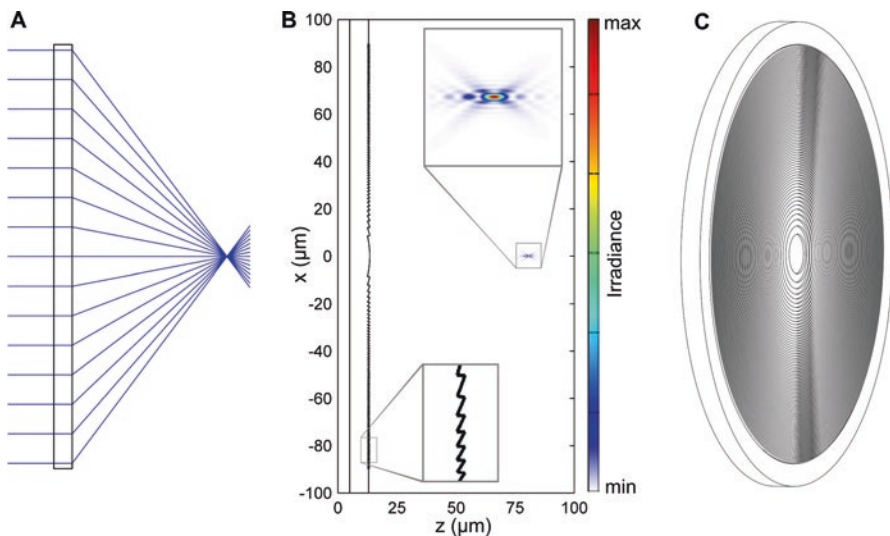


Fig. 6.13 Diffractive lens to be printed via multiphoton lithography. (a) Optical design for a wavelength = 543 nm and NA of 0.8. (b) Physical optical simulation of the profile via WPM propagation. (c) Corresponding CAD model

corresponding CAD model can be determined via modulo operation with the above step height. For this example, the resulting minimum period of the diffractive structure is about 700 nm at an ideal step height of 990 nm.

In a second step, the diffractive lens was printed, and the performance was assessed experimentally. The PSF was measured using a collimated laser beam under perpendicular incidence at the design wavelength. The spot in the focus was imaged with a microscope (100 \times objective with NA = 0.8). Figure 6.14 shows the result of the experiment in comparison with simulation. The resulting full widths at half maximum (FWHM) values are 303 nm (ZEMAX), 336 nm (WPM), and 452 nm (experimental, average of x- and y-section). In the diffraction limit, this corresponds to effective numerical apertures of 0.8 (ZEMAX), 0.75 (WPM), and 0.6 (experiment). It is assumed that the difference between simulation and experiment results from the unavoidable profile shape deviation, which however could be partly counter-compensated via profile optimization [69]. In summary the experiment proves that focusing into a subwavelength-sized spot is feasible with printed diffractive elements.

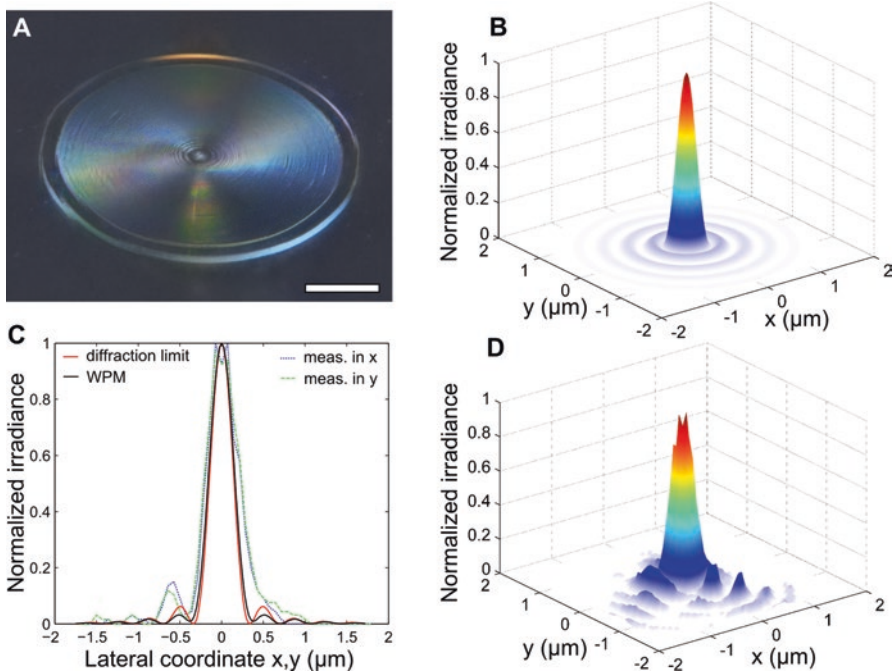


Fig. 6.14 Experimental results of a printed diffractive lens. (a) Microscopic image (scale bar: 50 μm). (b) WPM-simulated PSF. (c) Comparison of the diffraction-limited PSF versus the WPM and the experimental data. Resulting FWHM values: 303 nm (ZEMAX), 336 nm (WPM), and 452 nm (average of x- and y-profile). (d) Experimentally retrieved PSF

While the above examples were optimized for a point source or a point focus, we now are investigating a printed illumination system for an extended source². Light-emitting diode (LED) light sources, in comparison to mono-mode lasers or fibers, exhibit a large-area angle product, or étendue. This results from the large angular emission characteristics in combination with an extended emitter area. The considerably large étendue limits the achievable level of collimation, especially if the collimator must be small in volume/diameter and close to the source. In consequence the collimation angle which can be realized with a printed microoptical component is limited, but nevertheless a reduction of the angular spectrum is possible.

We illustrate this with the following TIR collimation element, which was printed on top of an LED emitter surface and was able to reduce the angular radiation angle from 60° to 31.4° (Fig. 6.15). The emitter was a so-called Point Source LED (OSRAM F1372B), which is characterized by a very small emission area of only $80\ \mu\text{m}$ in diameter at a wavelength of $650\ \text{nm}$ ($20\ \text{nm}$ FWHM spectral width).

For the geometry of the TIR collimator, a combination of a dielectric total internal reflecting concentrator (DTIRC) and an aspherical surface was selected, as illustrated in Fig. 6.15. For the experimental verification, an LED of the TO-18 package was used, which allows for a simple handling, printing, and processing. As print material the standard photoresist IP-S was employed, which generally results in smooth printed surfaces. Figure 6.16 shows microscope images of the printed geometries. The angular emission characteristics of the light source were measured before and after the printing process, each time with the same driving current of $10\ \text{mA}$. As a test setup, the LED was placed under a Lambertian diffusor screen at $30\ \text{mm}$, far enough to neglect the spatial extent of the light source. The irradiance

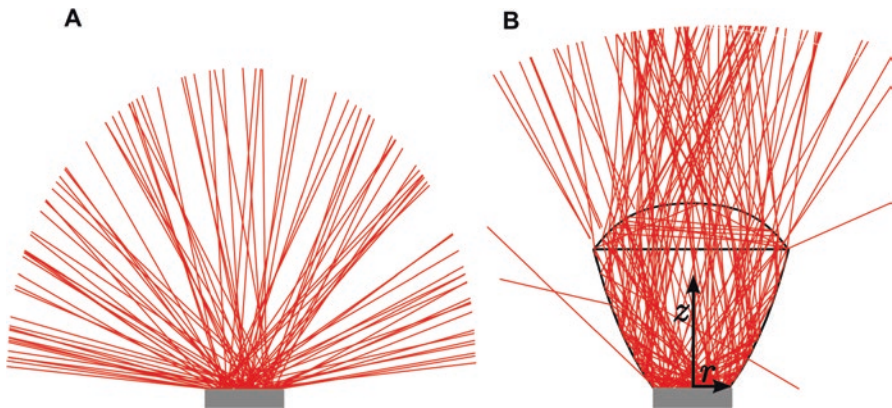


Fig. 6.15 (a) Intensity characteristics of the “Point Source LED” alone. (b) Reduced angular intensity width of the same source in combination with a printed TIR collimator. Reprinted with permission from reference [70]

²The corresponding results were published before in [70].

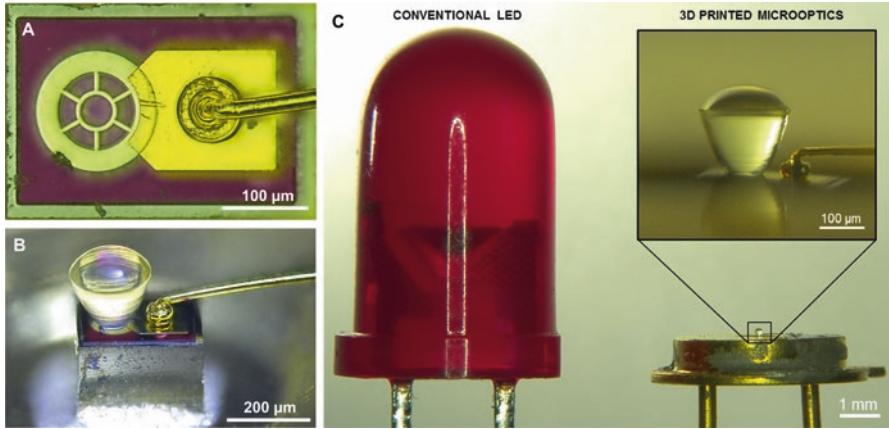


Fig. 6.16 Results of the 3D printing process. (a) “Point Source” LED chip before processing. (b) Chip after printing of a TIR collimator. (c) Comparison to a standard LED. Reprinted with permission from reference [70]

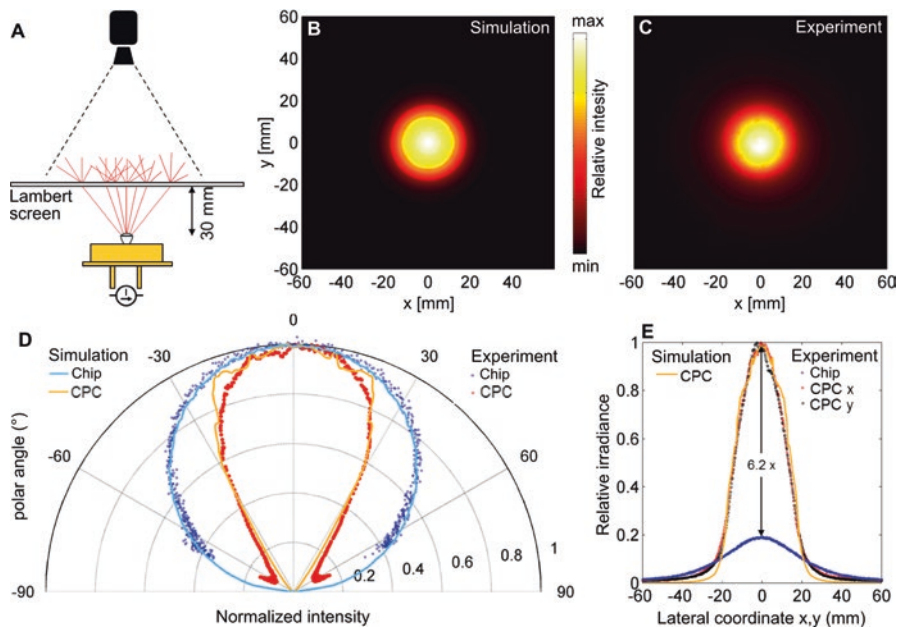


Fig. 6.17 Radiometric analysis and comparison to simulation. (a) Test setup for radiometric measurements. (b) Simulated irradiance on the diffusor in 30 mm distance. (c) Measured irradiance distribution. (d) Comparison of the normalized simulated and measured angular characteristics. (e) Corresponding relative irradiance profiles. Reprinted with permission from reference [70]

distribution on the diffusor was recorded with a standard color DSLR camera. The image was converted into gray levels by simple addition of the intensity of the three different color channels.

Again, a comparison between simulation and experimental results was performed. To do so, a nonsequential simulation model, containing the emission area and the TIR geometry, was set up in ZEMAX. Figure 6.17 shows the comparison of simulation results to the experimental results. Overall a very good match between both was achieved. The results predict that the printed collimation system can reduce the angular width from 60° to $\sim 30^\circ$. The slight differences between simulation and experiment can most likely be explained by the remaining surface roughness on the TIR surface.

6.5 Summary

The fabrication method of femtosecond direct laser writing enables the 3D printing of complex optical components and systems. Due to its many degrees of freedom in terms of optical and structural design, specific rules were developed and introduced specifically for imaging systems. Two examples of doublet imaging objectives are presented and compared in design, fabrication, and imaging performance. A method which allows the direct assembly-free integration of absorbing structures is introduced and demonstrated experimentally. As three examples for nonimaging optics, coupling lenses for quantum dots, a diffractive lens for sub- μm focusing, and a collimation structure for LEDs are presented.

References

1. Wu E.-S., Strickler J. H., Harrell W. R., & Webb W. W. (1992). Two-photon lithography for microelectronic application. In *SPIE Proceedings* (p. 776). SPIE.
2. Maruo, S., Nakamura, O., & Kawata, S. (1997). Three-dimensional microfabrication with two-photon-absorbed photopolymerization. *Optics Letters*, 22, 132.
3. Maruo, S., & Kawata, S. (1998). Two-photon-absorbed near-infrared photopolymerization for three-dimensional microfabrication. *Journal of Microelectromechanical Systems*, 7, 411–415.
4. Sun, H.-B., Matsuo, S., & Misawa, H. (1999). Three-dimensional photonic crystal structures achieved with two-photon-absorption photopolymerization of resin. *Applied Physics Letters*, 74, 786–788.
5. Serbin, J., Egbert, A., Ostendorf, A., Chichkov, B. N., Houbertz, R., Domann, G., Schulz, J., Cronauer, C., Fröhlich, L., & Popall, M. (2003). Femtosecond laser-induced two-photon polymerization of inorganic-organic hybrid materials for applications in photonics. *Optics Letters*, 28, 301.
6. Straub, M., & Gu, M. (2002). Near-infrared photonic crystals with higher-order bandgaps generated by two-photon photopolymerization. *Optics Letters*, 27, 1824.
7. Korte, F., Serbin, J., Koch, J., Egbert, A., Fallnich, C., Ostendorf, A., & Chichkov, B. N. (2003). Towards nanostructuring with femtosecond laser pulses. *Applied Physics A*, 77, 229–235.

8. Straub, M., Nguyen, L. H., Fazlic, A., & Gu, M. (2004). Complex-shaped three-dimensional microstructures and photonic crystals generated in a polysiloxane polymer by two-photon microstereolithography. *Optical Materials*, 27, 359–364.
9. Serbin, J., Ovsianikov, A., & Chichkov, B. (2004). Fabrication of woodpile structures by two-photon polymerization and investigation of their optical properties. *Optics Express*, 12, 5221.
10. Deubel, M., Wegener, M., Linden, S., von Freymann, G., & John, S. (2006). 3D-2D-3D photonic crystal heterostructures fabricated by direct laser writing. *Optics Letters*, 31, 805.
11. Deubel, M., von Freymann, G., Wegener, M., Pereira, S., Busch, K., & Soukoulis, C. M. (2004). Direct laser writing of three-dimensional photonic-crystal templates for telecommunications. *Nature Materials*, 3, 444–447.
12. Guo, R., Li, Z., Jiang, Z., Yuan, D., Huang, W., & Xia, A. (2005). Log-pile photonic crystal fabricated by two-photon photopolymerization. *Journal of Optics A: Pure and Applied Optics*, 7, 396–399.
13. Wu, S., Serbin, J., & Gu, M. (2006). Two-photon polymerisation for three-dimensional micro-fabrication. *Journal of Photochemistry and Photobiology A: Chemistry*, 181, 1–11.
14. Gan, Z., Cao, Y., Evans, R. A., & Gu, M. (2013). Three-dimensional deep sub-diffraction optical beam lithography with 9 nm feature size. *Nature Communications*, 4, 2061.
15. Fischer, J., & Wegener, M. (2013). Three-dimensional optical laser lithography beyond the diffraction limit. *Laser & Photonics Reviews*, 7, 22–44.
16. Chidambaram, N., Kirchner, R., Fallica, R., Yu, L., Altana, M., & Schiff, H. (2017). Selective surface smoothening of polymer microlenses by depth confined softening. *Advanced Materials Technologies*, 2, 1700018.
17. Sun H.-B., & Kawata S. (2004). Two-photon photopolymerization and 3d lithographic micro-fabrication. In *NMR • 3D Analysis • Photopolymerization* (Vol. 170, pp. 169–273). Berlin, Springer.
18. Yang, D., Jhaveri, S. J., & Ober, C. K. (2005). Three-dimensional microfabrication by two-photon lithography. *MRS Bulletin*, 30, 976–982.
19. Wippermann F. C., Radtke D., Zeitner U., Duparré J. W., Tünnermann A., Amberg M., Sinzinger S., Reinhardt C., Ovsianikov A., & Chichkov B. N.. (2006). Fabrication technologies for chirped refractive microlens arrays. In *SPIE Proceedings* (p. 628800). SPIE.
20. Ostendorf, A., & Chichkov, B. N. (2006). Two-photon polymerization: a new approach to micromachining. *Photonics Spectra*, 40, 72–80.
21. Guo, R., Xiao, S., Zhai, X., Li, J., Xia, A., & Huang, W. (2006). Micro lens fabrication by means of femtosecond two photon photopolymerization. *Optics Express*, 14, 810.
22. Chen, Q.-D., Wu, D., Niu, L.-G., Wang, J., Lin, X.-F., Xia, H., & Sun, H.-B. (2007). Phase lenses and mirrors created by laser micronanofabrication via two-photon photopolymerization. *Applied Physics Letters*, 91, 171105.
23. Nishiyama, H., Nishii, J., Mizoshiri, M., & Hirata, Y. (2009). Microlens arrays of high-refractive-index glass fabricated by femtosecond laser lithography. *Applied Surface Science*, 255, 9750–9753.
24. Wu, D., Wu, S.-Z., Niu, L.-G., Chen, Q.-D., Wang, R., Song, J.-F., Fang, H.-H., & Sun, H.-B. (2010). High numerical aperture microlens arrays of close packing. *Applied Physics Letters*, 97, 31109.
25. Malinauskas, M., Gilbergs, H., Žukauskas, A., Purlys, V., Paipulas, D., & Gadonas, R. (2010). A femtosecond laser-induced two-photon photopolymerization technique for structuring microlenses. *Journal of Optics*, 12, 35204.
26. Žukauskas, A., Malinauskas, M., Reinhardt, C., Chichkov, B. N., & Gadonas, R. (2012). Closely packed hexagonal conical microlens array fabricated by direct laser photopolymerization. *Applied Optics*, 51, 4995–5003.
27. Hu, Y., Chen, Y., Ma, J., Li, J., Huang, W., & Chu, J. (2013). High-efficiency fabrication of aspheric microlens arrays by holographic femtosecond laser-induced photopolymerization. *Applied Physics Letters*, 103, 141112.

28. Malinauskas, M., Žukauskas, A., Purlys, V., Belazaras, K., Momot, A., Paipulas, D., Gadonas, R., Piskarskas, A., Gilbergs, H., Gaidukevičiūtė, A., Sakellari, I., Farsari, M., & Juodkazis, S. (2010). Femtosecond laser polymerization of hybrid/integrated micro-optical elements and their characterization. *Journal of Optics*, *12*, 124010.
29. Brasselet, E., Malinauskas, M., Žukauskas, A., & Juodkazis, S. (2010). Photopolymerized microscopic vortex beam generators. Precise delivery of optical orbital angular momentum. *Applied Physics Letters*, *97*, 211108.
30. Malinauskas, M., Žukauskas, A., Belazaras, K., Tikuišis, K., Purlys, V., Gadonas, R., & Piskarskas, A. (2012). Laser fabrication of various polymer microoptical components. *European Physical Journal Applied Physics*, *58*, 20501.
31. Osipov, V., Doskolovich, L. L., Bezus, E. A., Cheng, W., Gaidukeviciute, A., & Chichkov, B. (2012). Fabrication of three-focal diffractive lenses by two-photon polymerization technique. *Applied Physics A: Materials Science & Processing*, *107*, 525–529.
32. Thiel M, Radke A., Fries B., Eicke D., Niesler F., Baretzky C., Bückmann T., & Wegener M. (2013). High-speed 3D direct laser writing of micro-optical elements. in CLEO: Science and Innovations. Part of Conference on Lasers and Electro-Optics, 9–14 May 2013. San Jose, CA, OSA technical digest (online): OSA The Optical Society, ATu2N.4.
33. Malinauskas, M., Farsari, M., Piskarskas, A., & Juodkazis, S. (2013). Ultrafast laser nanostructuring of photopolymers. A decade of advances. *Physics Reports*, *533*, 1–31.
34. Schumann, M., Bückmann, T., Gruhler, N., Wegener, M., & Pernice, W. (2014). Hybrid 2D–3D optical devices for integrated optics by direct laser writing. *Light: Science and Applications*, *3*, e175.
35. Lightman, S., Hurvitz, G., Gvishi, R., & Arie, A. (2017). Tailoring lens functionality by 3{D} laser printing. *Applied Optics*, *56*, 9038–9043.
36. Lightman, S., Hurvitz, G., Gvishi, R., & Arie, A. (2017). Miniature wide-spectrum mode sorter for vortex beams produced by 3{D} laser printing. *Optica*, *4*, 605.
37. Williams, H. E., Freppon, D. J., Kuebler, S. M., Rumpf, R. C., & Melino, M. A. (2011). Fabrication of three-dimensional micro-photon structures on the tip of optical fibers using SU-8. *Optics Express*, *19*, 22910–22922.
38. Žukauskas, A., Malinauskas, M., & Brasselet, E. (2013). Monolithic generators of pseudo-nondiffracting optical vortex beams at the microscale. *Applied Physics Letters*, *103*, 181122.
39. Žukauskas, A. (2014). Improvement of the fabrication accuracy of fiber tip microoptical components via mode field expansion. *Journal of Laser Micro/Nanoengineering*, *9*, 68–72.
40. Gissibl, T., Thiele, S., Herkommer, A., & Giessen, H. (2016). Two-photon direct laser writing of ultracompact multi-lens objectives. *Nature Photonics*, *10*, 554–560.
41. Weiss I., & Marom D. M. (2016). Direct 3D nanoprinting on fiber tip of collimating lens and OAM mode converter in one compound element. In *2016 Optical Fiber Communications Conference and Exhibition (OFC)* (p. Th3E.2), 20–24 March 2016. IEEE.
42. Cojoc, G., Liberale, C., Candeloro, P., Gentile, F., Das, G., de Angelis, F., & Di Fabrizio, E. (2010). Optical micro-structures fabricated on top of optical fibers by means of two-photon photopolymerization. *Microelectronic Engineering*, *87*, 876–879.
43. Bianchi, S., Rajamanickam, V. P., Ferrara, L., Di Fabrizio, E., Liberale, C., & Di Leonardo, R. (2013). Focusing and imaging with increased numerical apertures through multimode fibers with micro-fabricated optics. *Optics Letters*, *38*, 4935–4938.
44. Gissibl, T., Thiele, S., Herkommer, A., & Giessen, H. (2016). Sub-micrometre accurate free-form optics by three-dimensional printing on single-mode fibres. *Nature Communications*, *7*, 11763.
45. Weiss I., & Marom D. M. (2015). Direct 3D nano-printing on optical fiber tip. In *2015 International Conference on Optical MEMS and Nanophotonics, 2–5 August 2015* (pp. 1–2). Jerusalem: OMN2015, Jerusalem: proceedings. IEEE.
46. Malinauskas, M., Žukauskas, A., Purlys, V., Gaidukevičiūtė, A., Balevičius, Z., Piskarskas, A., Fotakis, C., Pissadakis, S., Gray, D., Gadonas, R., Vamvakaki, M., & Farsari, M. (2012). 3D microoptical elements formed in a photostructurable germanium silicate by direct laser writing. *Optics and Lasers in Engineering*, *50*, 1785–1788.

47. Gissibl, T., Schmid, M., & Giessen, H. (2016). Spatial beam intensity shaping using phase masks on single-mode optical fibers fabricated by femtosecond direct laser writing. *Optica*, 3, 448.
48. Kowalczyk, M., Haberko, J., & Wasylczyk, P. (2014). Microstructured gradient-index anti-reflective coating fabricated on a fiber tip with direct laser writing. *Optics Express*, 22, 12545–12550.
49. Li, J., Fejes, P., Lorensen, D., Quirk, B. C., Noble, P. B., Kirk, R. W., Orth, A., Wood, F. M., Gibson, B. C., Sampson, D. D., & McLaughlin, R. A. (2018). Two-photon polymerisation 3D printed freeform micro-optics for optical coherence tomography fibre probes. *Scientific Reports*, 8, 14789.
50. Lightman, S., Gvishi, R., Hurvitz, G., & Arie, A. (2015). Shaping of light beams by 3D direct laser writing on facets of nonlinear crystals. *Optics Letters*, 40, 4460–4463.
51. Schleunitz A., Klein J. J., Houbertz R., & Krupp A. (2017). Novel hybrid polymers for fabrication of advanced micro-optics. In *SPIE Newsroom*. SPIE.
52. Sun, Y.-L., Dong, W.-F., Niu, L.-G., Jiang, T., Liu, D.-X., Zhang, L., Wang, Y.-S., Chen, Q.-D., Kim, D.-P., & Sun, H.-B. (2014). Protein-based soft micro-optics fabricated by femtosecond laser direct writing. *Light: Science and Applications*, 3, e129.
53. Kotz, F., Plewa, K., Bauer, W., Schneider, N., Keller, N., Nargang, T., Helmer, D., Sachsenheimer, K., Schäfer, M., Worgull, M., Greiner, C., Richter, C., & Rapp, B. E. (2016). Liquid glass: a facile soft replication method for structuring glass. *Advanced Materials (Deerfield Beach, Fla.)*, 28, 4646–4650.
54. Cadarso, V. J., Perera-Núñez, J., Jacot-Descombes, L., Pfeiffer, K., Ostrzinski, U., Voigt, A., Llobera, A., Grützer, G., & Brugger, J. (2011). Microlenses with defined contour shapes. *Optics Express*, 19, 18665–18670.
55. Cheng, Y., Sugioka, K., Midorikawa, K., Masuda, M., Toyoda, K., Kawachi, M., & Shihoyama, K. (2003). Three-dimensional micro-optical components embedded in photo-sensitive glass by a femtosecond laser. *Optics Letters*, 28, 1144.
56. Gale M. T., & Knop K. (1983). The fabrication of fine lens arrays by laser beam writing. In *SPIE Proceedings* (pp. 347–353). SPIE.
57. Göppert-Mayer, M. (1931). Über Elementarakte mit zwei Quantensprüngen. *Ann. Phys.*, 401, 273–294.
58. Spence, D. E., Kean, P. N., & Sibbett, W. (1991). 60-fsec pulse generation from a self-mode-locked Ti: Sapphire laser. *Optics Letters*, 16, 42.
59. Sibbett, W., Lagatsky, A. A., & Brown, C. T. A. (2012). The development and application of femtosecond laser systems. *Optics Express*, 20, 6989–7001.
60. Jeff's M. (2002). Reduced manufacturing sensitivity in multi-element lens systems. In *SPIE Proceedings* (p. 104). SPIE.
61. Isshiki M., Sinclair D. C., & Kaneko S. (2006). *Lens design. Global optimization of both performance and tolerance sensitivity* (Vol. 6342, p. 63420N). International Society for Optics and Photonics.
62. Bates R.. (2010). Performance and tolerance sensitivity optimization of highly aspheric miniature camera lenses. In *SPIE Proceedings* (p. 779302). SPIE.
63. Ruffieux, P., Scharf, T., Herzig, H. P., Völkel, R., & Weible, K. J. (2006). On the chromatic aberration of microlenses. *Optics Express*, 14, 4687.
64. Rill, M. S., Krieglger, C. E., Thiel, M., von Freymann, G., Linden, S., & Wegener, M. (2009). Negative-index bianisotropic photonic metamaterial fabricated by direct laser writing and silver shadow evaporation. *Optics Letters*, 34, 19.
65. Ma, Z.-C., Zhang, Y.-L., Han, B., Chen, Q.-D., & Sun, H.-B. (2018). Femtosecond-laser direct writing of metallic micro/nanostructures. From fabrication strategies to future applications. *Small Methods*, 2, 1700413.
66. Fischbach, S., Schlehahn, A., Thoma, A., Srocka, N., Gissibl, T., Ristok, S., Thiele, S., Kaganskiy, A., Strittmatter, A., Heindel, T., Rodt, S., Herkommer, A., Giessen, H., & Reitzenstein, S. (2017). Single quantum dot with microlens and 3D-printed micro-objective as integrated bright single-photon source. *ACS Photonics*, 4, 1327–1332.

67. Schmidt, S., Tiess, T., Schröter, S., Hambach, R., Jäger, M., Bartelt, H., Tünnermann, A., & Gross, H. (2016). Wave-optical modeling beyond the thin-element-approximation. *Optics Express*, *24*, 30188–30200.
68. Schmidt, S., Thiele, S., Herkommer, A., Tünnermann, A., & Gross, H. (2017). Rotationally symmetric formulation of the wave propagation method-application to the straylight analysis of diffractive lenses. *Optics Letters*, *42*, 1612–1615.
69. Korolkov, V. P., Nasyrov, R. K., & Shimansky, R. V. (2006). Zone-boundary optimization for direct laser writing of continuous-relief diffractive optical elements. *Applied Optics*, *45*, 53.
70. Thiele, S., Gissibl, T., Giessen, H., & Herkommer, A. M. (2016). Ultra-compact on-chip LED collimation optics by 3D femtosecond direct laser writing. *Optics Letters*, *41*, 3029–3032.